Kovove Mater. 55 2017 369–378
DOI: 10.4149/km_2017_6_369

Effect of anisotropic microstructure on high-temperature compression deformation of CoCrFeNi based complex concentrated alloy

M. Štamborská*, J. Lapin

Institute of Materials & Machine Mechanics, Slovak Academy of Sciences, Dúbravská cesta 9, 845 13 Bratislava, Slovak Republic

Received 21 August 2017, received in revised form 10 October 2017, accepted 12 October 2017

Abstract

The effect of anisotropic as-cast microstructure on high-temperature compression deformation of multiphase $Co_{24}Cr_{19}Fe_{24}Ni_{19}Al_8(Ti,Si,C)_6$ (at.%) complex concentrated alloy (CCA) derived from a single phase CoCrFeNi based high entropy alloy (HEA) was studied at temperatures ranging from 750 to 900 °C. The highly anisotropic microstructure composed of several columnar grains with [100] crystallographic direction parallel or nearly parallel to the load axis leads to asymmetric barrelled shapes of the compression specimens with multiple protuberances on the barrelled surfaces. The experimental barrelled shapes differ from the numerically calculated ones. The deformation curves exhibit strain hardening stage which is followed by a deformation at a constant flow stress at all studied temperatures. The work hardening rate (WHR) first increases with increasing strain. After achieving a peak value, the WHR decreases and achieves values around zero corresponding to the steady-state deformation. The finite element analysis (FEA) of 3D distribution of local equivalent strains and stresses corresponds qualitatively quite well to the observed structural changes within the barrelled specimens.

K e y w o r d s: complex concentrated alloys, high-entropy alloys, anisotropy, plastic deformation, mechanical properties, finite element modelling

1. Introduction

Nuclear, turbine, and aerospace industries currently place high demands on high-temperature structural alloy properties and look for materials that could be superior to conventional nickel-based superalloys. In the last decade, a new class of materials, called high-entropy alloys (HEAs) and related concepts (multi-principal-element alloys – MPEAs and complex concentrated alloys – CCAs), have been proposed and developed [1–5]. The basic concept behind the design of HEAs is to promote the formation of single phase disordered solid solutions containing five or more principal elements which are stabilised by configurational entropy. On the other hand, the more recent concept of CCAs is based on the requirement that the alloy composition is positioned in the central region of the multi-dimensional phase diagram of multicomponent alloys and formation of more phases is possible [4]. Existing literature reviews on the HEAs focus on the search for a simple solid solution containing only fcc, bcc, and hcp structures [1–3]. However, mechanical properties of single phase HEAs are controlled only by three strengthening mechanisms: (i) solid solution hardening, (ii) work-hardening and (iii) grain size. These mechanisms become less effective at high temperatures due to recovery, recrystallisation, grain growth, and diffusive drag of solute atoms which leads to a significant softening and insufficient strength for high-temperature structural applications [6, 7]. It is often stated that the motivation for the design of HEAs is to avoid the formation of intermetallic phases, which might embrittle structural alloys. However, the best balance of strength and damage tolerance is found in structural materials that rely on significant volume fractions of intermetallic or ceramic phases. Since the knowledge regarding the control and stability of intermetallic and ceramic phases in HEAs is still very

*Corresponding author: tel.: +421 2 3240 1058; e-mail address: michaela.stamborska@savba.sk

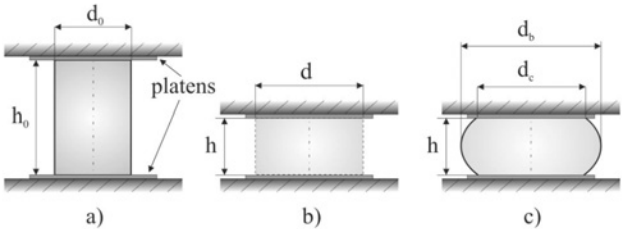

Fig. 1. Schema of compression specimen: (a) cylindrical specimen before deformation; (b) cylindrical shape after deformation without friction; (c) barrelled shape after deformation with friction.

limited, the design of multiphase CCAs reinforced by these phases is very difficult [1, 8, 9]. Among various HEAs, the outstanding ductility of CoCrFeNi based alloy can serve as a good base for the design of CCAs strengthened by intermetallic and ceramic phases for high-temperature structural applications. He et al. [9] have reported outstanding tensile properties of the alloy with nominal composition $(FeCoNiCr)_{94}Ti_2Al_4$ (at.%), which has been achieved by precipitation of nanosized $L1_2$-Ni_3(Ti,Al) particles in a fcc-FeCoNiCr HEA matrix. Although the authors have designated the studied FeCoNiCr alloy as HEA, this system corresponds better to the recent concept of CCAs because it contains only four main alloying elements and the rule of the single solid solution is not respected [9].

The newly developed CCAs reinforced with intermetallic and ceramic phases meeting the requirements for production need to be subjected to hot working processes after solidification. Therefore, it is necessary to understand the effect of specific as-cast microstructures on their deformation behaviour and microstructure evolution at high temperatures. Experimental characterisation of deformation behaviour of materials is complicated by the fact that deformation becomes non-uniform within the tested specimens. This non-uniformity is accompanied with a necking in tension [10–12] and barrelling in compression [13–18]. Both the necking and barrelling represent local plastic instabilities that depend not only on intrinsic material properties but specimen geometry as well. Compression tests are widely used to obtain elevated temperature deformation behaviour of various materials. Intrinsic material properties and friction at the interfaces between the compression specimen and the platens is a source of strain inhomogeneity in the compression specimen and results in the barrelling causing a triaxial stress state during deformation, as seen in Fig. 1.

The present article aims to study the effect of anisotropic as-cast microstructure on high-temperature compression deformation of multiphase complex concentrated alloy with additions of Al, Ti, Si, and C derived from a single phase CoCrFeNi based high entropy alloy. The compression tests are carried out with a Gleeble thermomechanical simulator, and finite element analysis (FEA) is applied for 3D numerical modelling of equivalent strains and stresses within barrelled compression specimens.

2. Experimental material and procedures

The studied CoCrFeNi based alloy with the additions of Al, Ti, Si, and C was prepared from master alloys by induction melting in a vacuum induction furnace. Before melting the vacuum chamber of the medium frequency induction furnace was evacuated to 5.5 Pa, flushed with argon three times and finally filled with argon (purity of 99.9995 %) to a pressure of 2 kPa. The charge was heated to a melt temperature of 1500 ℃ and hold at this temperature for 180 s to achieve full dissolution of all alloying elements. The temperature of the melt was measured by a pyrometer. The gravity casting was carried out in the vacuum chamber under an argon pressure of 2 kPa. The as-cast bar with a diameter of 38 mm and length of 180 mm was cut in a direction parallel to its longitudinal axis to smaller cylindrical samples with a diameter of 7 mm and length of 150 mm by wire electrical discharge machining. Compression specimens with a diameter of 6 mm and length of 9 mm were prepared by lathe machining. The surface of the specimens was polished to a roughness better than 0.3 μm.

Compression tests were carried out at an initial strain rate of $10^{-1}\,s^{-1}$ and four temperatures of 750, 800, 850, and 900 ℃ using a Gleeble thermomechanical tester 3800 under a vacuum of 7 Pa. Tantalum foil with nickel paste was used to minimise the friction between platens and the specimen. The test temperature was measured by a thermocouple touching the specimen surface. The specimens were heated to test temperature at a rate of $6.7\,℃\,s^{-1}$ and held at the temperature for 120 s. After the compression test to an engineering strain of 0.4, each specimen was cooled to room temperature in air. The compression tests were carried out on five specimens at each test temperature, and twenty compression specimens in total were tested.

The software Ansys Workbench was used for numerical simulation. A geometry model was built as a 3D cylinder with a diameter of 6 mm and height of 9 mm. Two compression platens were modelled as 3D plates. Triaxial stress distribution was assumed to occur due to friction between the platens and compression specimen, and 3D analysis was used instead of axisymmetric one. Material model was built up using the achieved experimental data from the Gleeble compression tests. For 3D analysis, deformable hexahedron elements with a size of 0.35 and 0.75 mm were used to mesh the cylindrical compression specimen and platens, respectively, as seen in Fig. 2.

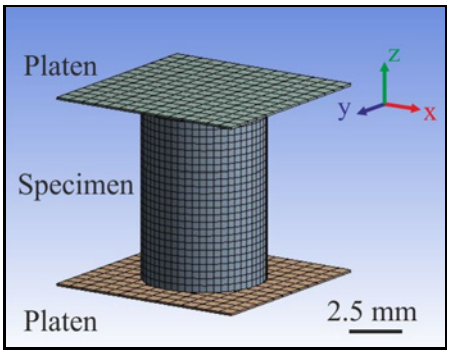

Fig. 2. The initial mesh of compression model obtained by finite element analysis.

Microstructure evaluation was performed by optical microscopy (OM), scanning electron microscopy (SEM) in backscattered electron (BSE) mode and energy-dispersive X-ray spectroscopy (EDS). Metallographic preparation of the samples consisted of standard grinding using abrasive papers and polishing on diamond pastes with various grain size up to 1 µm. OM samples were etched in a reagent of 20 ml HNO_3, 20 ml H_2O, 20 ml HF and few drops of H_2SO_4.

3. Results and discussion

3.1. Microstructure of the as-cast alloy

The microstructure of the as-cast bar with the measured average chemical composition corresponding to $Co_{24}Cr_{19}Fe_{24}Ni_{19}Al_8(Ti,Si,C)_6$ (at.%) is highly anisotropic, as shown in Fig. 3. The typical structure consists of fine grains formed in the vicinity of the bar surface followed by large columnar grains elongated towards the centre (Fig. 3a) and the equiaxed grains formed in the centre of the bar (Fig. 3b). Liu et al. [19] have reported that the primary solidification phase of CoCrFeNiAl HEA is the solid solution either with fcc or bcc crystal structure depending on the content of Al. Although a detailed phase analysis of the studied alloy has not been carried out for this work, the measured content of Al supports the assumption that the primary solidification phase is fcc solid solution [19]. Figure 3b shows clearly cubic symmetry of the dendrites with the typical "maltese cross" on a transverse section of the as-cast bar cut perpendicularly to its longitudinal axis. As reported for various alloys, the fcc or bcc primary dendrites grow in [001] crystallographic direction which is close to the heat transfer direction during the solidification [20–24]. In the case of the studied CCA, the [001] crystallographic direction of the columnar dendrites is perpendicular or nearly perpendicular to the longitudinal axis of the as-cast bar.

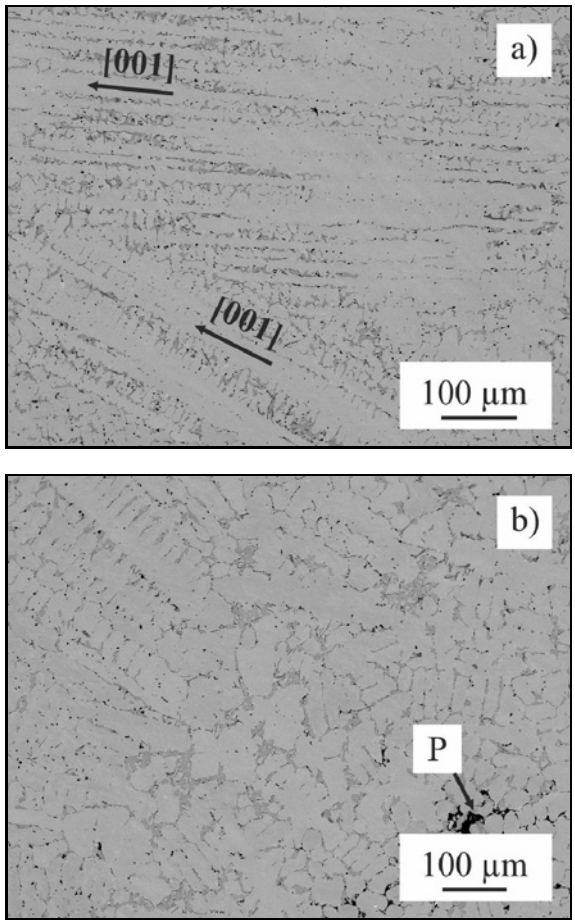

Fig. 3. BSE micrographs showing a transversal section of the as-cast bar: (a) high angle grain boundary between two columnar dendritic grains at a distance of 2 mm from the surface of the bar; (b) columnar to equiaxed transition at a distance of 17 mm from the surface of the bar. P – porosity.

3.2. Initial microstructure of compression specimens

The columnar dendritic structure of the as-cast bar allowed to prepare compression specimens with highly anisotropic microstructure. In the present study, the longitudinal axis of the cylindrical compression specimens is parallel to the load axis and oriented nearly perpendicularly to the [001] crystallographic direction of the columnar dendrites, as shown in Fig. 4. Since each compression specimen consists of several columnar dendritic grains (3–6), the [100] crystallographic direction is parallel or nearly parallel to the load axis but [001] crystallographic direction of the individual grains is angularly rotated to each other (see an example of high angle boundary in Fig. 3a). Figure 4a indicates that some columnar dendrites are oriented at an angle close to 90° to the load axis. The secondary phases formed between the columnar dendrites

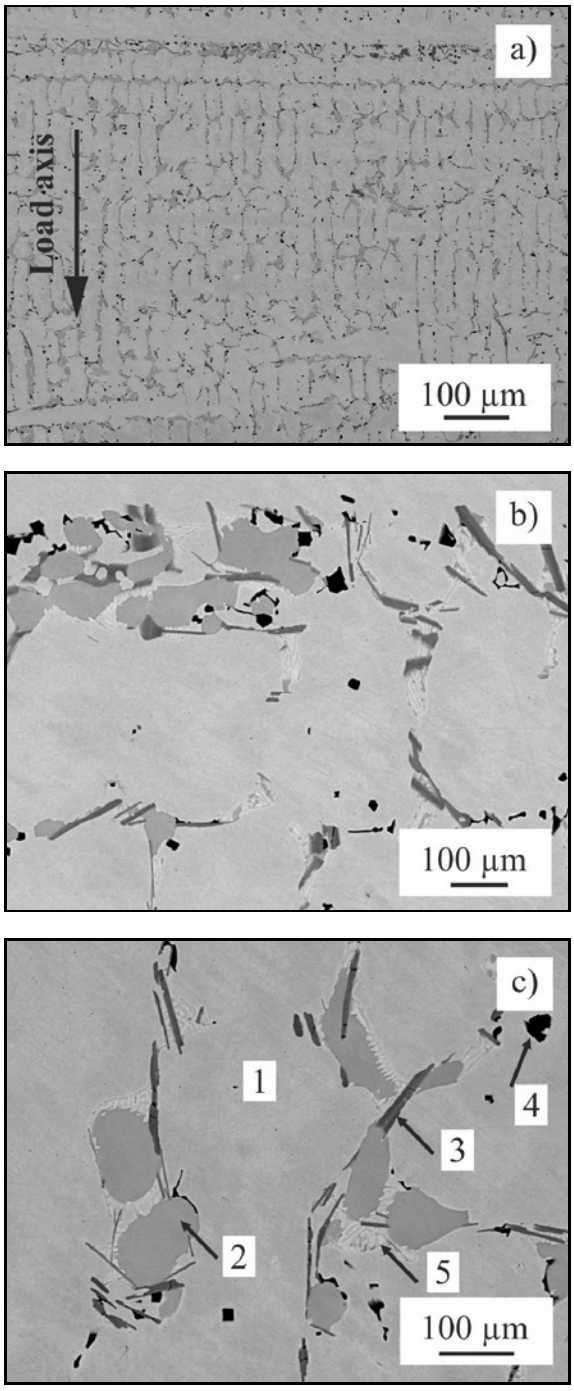

Fig. 4. BSE micrographs showing a longitudinal section of the compression specimen: (a) columnar dendrites oriented in a direction almost perpendicular to the load axis; (b) secondary phases formed between columnar dendrites; (c) secondary phases formed between secondary dendrite arms.

(Fig. 4b) or secondary dendrite arms (Fig. 4c) are arranged either in a nearly perpendicular or parallel way to the load axis, respectively. It should be noted that the heat transfer from the alloy poured in the cold mould has not been controlled during the solidification which resulted in some deviations of the [100] crystallographic direction of the load axis of the compression specimens which is found to vary from 0° to about 10°.

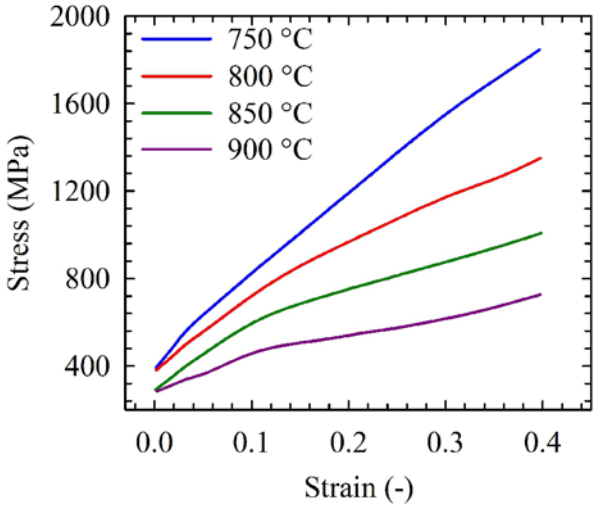

Fig. 5. Experimental engineering stress-strain curves. The test temperatures are indicated in the figure.

Five different phases with the chemical composition given in Table 1 can be well identified within the compression specimens. Based on the EDS measurements and recent work of Zhang et al. [25] and Joseph et al. [26], the primary solidification phase is the most probably fcc solid solution (region 1), as shown in Fig. 4c. The phase rich in Al (region 2) belongs probably to bcc or B2 phase [25, 26]. Minor additions of Ti, Si, and C lead to the formation of Cr-rich elongated particles (region 3) in the interdendritic region and coarse MC type of carbides (region 4) within the primary dendrites and in the interdendritic region. In addition, eutectic areas (5) enriched by Si are formed in the interdendritic region, as shown in Fig. 4c.

3.3. Deformation curves

Engineering stress-strain curves of the studied alloy compression tested at four temperatures are shown in Fig. 5. The engineering strain can be recalculated to true strain ε_t assuming the axial displacement Δh according to relationship [13]:

$$\varepsilon_t = \ln\left(\frac{h_0 + \Delta h}{h_0}\right), \tag{1}$$

where h_0 is the initial height of the compression specimen, h is the height of the deformed compression specimen and the displacement Δh is defined as $\Delta h = h - h_0$ (Figs. 1a,b). The true stress σ_t is calculated assuming constant volume and uniform plastic deformation of the cylindrical compression specimen

Table 1. EDS analysis of compression specimens

Region	Element (at.%)							
	Co	Cr	Fe	Ni	Al	Ti	Si	C
1	20.2 ± 0.3	24.4 ± 0.2	20.2 ± 0.2	23.9 ± 0.4	7.8 ± 0.3	0.8 ± 0.1	2.7 ± 0.2	–
2	17.6 ± 0.2	11.2 ± 0.2	11.2 ± 0.2	35.1 ± 0.4	24.7 ± 0.3	0.2 ± 0.1	–	–
3	17.1 ± 0.2	58.2 ± 0.3	11.2 ± 0.2	6.4 ± 0.2	1.1 ± 0.3	4.6 ± 0.1	1.4 ± 0.1	–
4	–	–	–	0.8 ± 0.2	1.5 ± 0.3	48.9 ± 0.4	–	48.8 ± 0.5
5	19.4 ± 0.2	21.4 ± 0.3	16.1 ± 0.2	27.8 ± 0.2	6.0 ± 0.3	–	9.3 ± 0.3	–

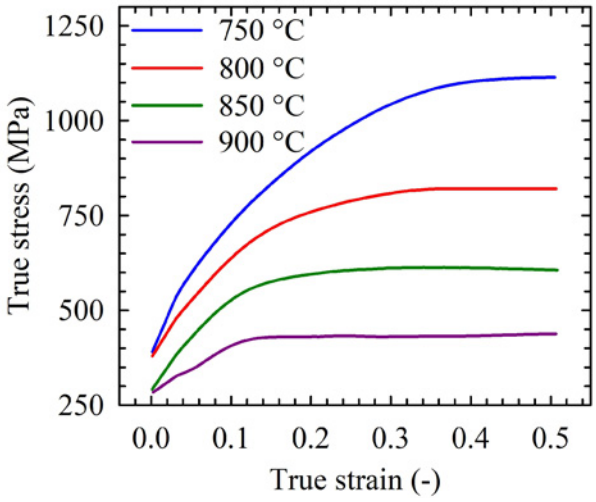

Fig. 6. True stress-true strain curves. The test temperatures are indicated in the figure.

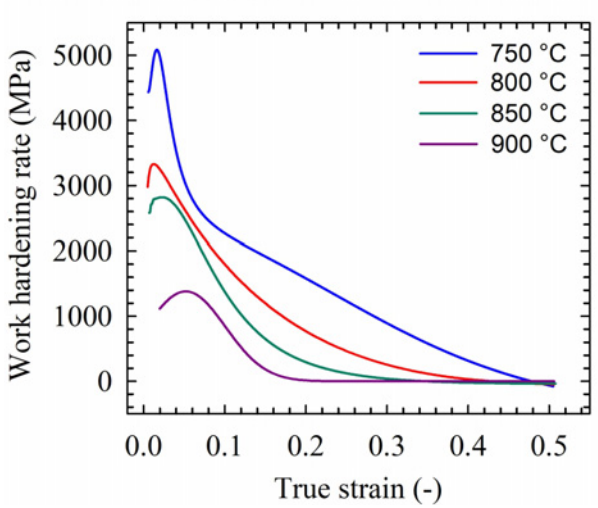

Fig. 7. Dependence of work hardening rate on the true strain. The test temperatures are indicated in the figure.

according to the relationship [13]:

$$\sigma_t = \frac{4F\,(h_0 + \Delta h)}{\pi d_0^2 h_0}, \qquad (2)$$

where F is the instantaneous applied force and d_0 is the initial diameter of the cylindrical compression specimen. Figure 6 shows the true stress-true strain curves of the studied alloy. The deformation curves exhibit strain hardening stage during which the true stress increases with increasing true strain. The strain hardening stage is followed by a steady-state stage characterised by a constant flow stress up to 0.51 true strain. The true strain, which is necessary for achieving the steady-state stress, depends strongly on the temperature and increases from 0.11 to 0.42 with decreasing the test temperature from 900 to 750 °C. The steady-state flow stress strongly depends on the temperature and decreases from 1111 to 437 MPa with the increase of the test temperature from 750 to 900 °C. The steady-state stage is characterised by a dynamic balance between the work hardening and work softening mechanisms operating during the high-temperature compression deformation. As reported by Wang et al. [27] and Samal et al. [28], the dislocation multiplication controls the work hardening behaviour, and dynamic recovery and dynamic recrystallisation are responsible for the dynamic softening at high temperatures.

Figure 7 shows the typical work-hardening rate (WHR) curves of the studied CCA. The WHR increases sharply with a strain, and when the strain reaches a critical value, the hardening rate decreases sharply due to the initiation of dynamic recovery and dynamic recrystallisation. It should be noted that the true strain corresponding to a peak hardening rate strongly depends on the temperature and decreases with decreasing temperature. After achieving a peak value, the strain hardening rate decreases with increasing strain and achieves values oscillating around zero that correspond to steady-state stage deformation represented by a constant flow stress.

3.4. Non-uniform deformation of compression specimens

The friction between the specimen and the platens causes the barrelling during compression deformation. Figure 1c shows a schema of barrelled compression specimen. Since it is very difficult to measure fric-

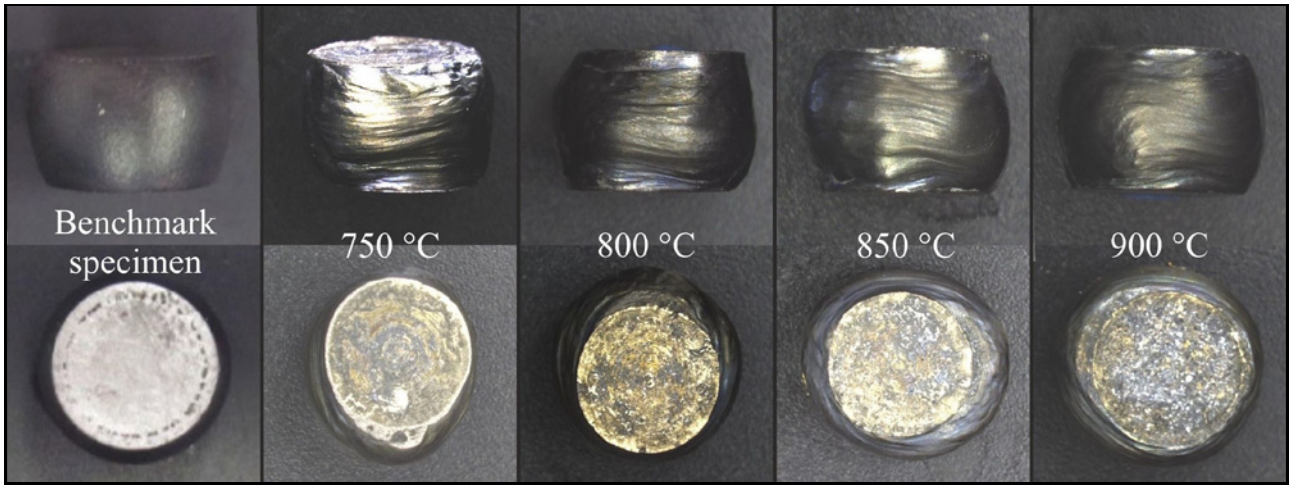

Fig. 8. The typical shapes of the barrelled specimens after Gleeble hot compression tests. The benchmark specimen is tested at 800 °C, and the test temperatures of the CCA specimens are indicated in the figures.

tion coefficient or friction force at high temperatures, an empirically determined friction coefficient ranging from 0.3 to 0.6 is frequently used. To include more accurately the friction into numerical modelling, an analytical method based on the barrelled shape of the compression specimens is used to calculate the friction coefficient μ [13, 29]:

$$\mu = \frac{m}{\sqrt{3}}, \tag{3}$$

where m is the average friction factor calculated as follows:

$$m = \frac{\frac{d}{2h}b}{\frac{4}{\sqrt{3}} - \frac{2b}{3\sqrt{3}}}, \tag{4}$$

where b is the barrelling parameter and d is the average diameter of the cylindrical specimen after the compression defined as:

$$d = d_0\sqrt{\frac{h_0}{h}}. \tag{5}$$

The barrelling parameter can be calculated as follows:

$$b = 4\frac{(d_\mathrm{b} - d_\mathrm{c})\, h^{1.5}}{\Delta h d_0 h_0^{0.5}} \tag{6}$$

where d_b is the maximum diameter, and d_c is the top diameter of the barrelled region of the compression specimen (Fig. 1c).

The anisotropic microstructure of the studied compression specimens affects significantly their non-uniform deformation behaviour accompanied with the barrelling. Figure 8 shows the typical barrelled shapes of the specimens after the compression tests at the test temperatures ranging from 750 to 900 °C. While the non-uniform deformation leads to a symmetric barrelling of a benchmark specimen made of a fine-grained ferritic-pearlitic steel [10, 11] at 800 °C, the asymmetric barrelled shapes are observed for the CCA specimens. While the deviations of the contact surfaces of the tested specimens from a regular circular shape are negligible, the barrelled region deviates significantly from this shape. The circularity of the barrelled region can be expressed by a shape factor S_b defined as [11]:

$$S_\mathrm{b} = \frac{4\pi A}{P^2}, \tag{7}$$

where A is the area, and P is the perimeter in the position of the barrelled region characterised by an average diameter d_b (see Fig. 1c). Figure 9 shows the temperature dependence of the friction coefficient μ and shape factor S_b calculated according to Eqs. (3) and (7), respectively. The deviation of the shape factor from 1 (circle) is caused by the highly anisotropic microstructure of the compression specimens containing several columnar grains oriented in [100] crystallographic direction parallel or nearly parallel to the load axis. The plastic deformation of fcc HEAs is controlled by a planar glide of dislocations on close-packed {111} planes and along the close-packed ⟨110⟩ directions at high temperatures [30–32]. Since the active {111}⟨110⟩ slip systems are oriented randomly to the load axis due to a random angular rotation of [001] crystallographic direction of the individual columnar grains, the non-uniform deformation leads to an asymmetric shape of the barrelled region.

The numerical modelling of the barrelling behaviour of the studied CCA by FEA is carried out using input material data from the compression tests and friction coefficients determined at the studied compression conditions using the procedure described

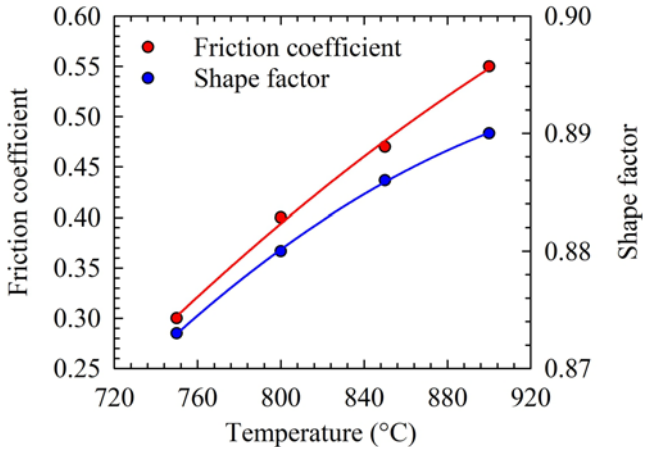

Fig. 9. Temperature dependence of the friction coefficient and shape factor.

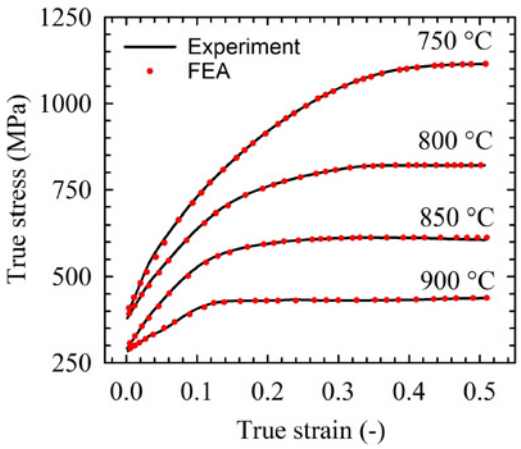

Fig. 10. True stress-true strain curves with the results from FEA. The test temperatures are indicated in the figure.

above. Figure 10 indicates that the results of numerical calculations are in a very good agreement with the experimentally measured true stress-true strain curves. The longitudinal sections of the barrelled specimens and corresponding 3D numerical calculations of equivalent plastic strains and equivalent (von Mises) stresses are shown in Fig. 11. It is clear that the barrelled shapes of the specimens (Figs. 11a,d,g,j) dif-

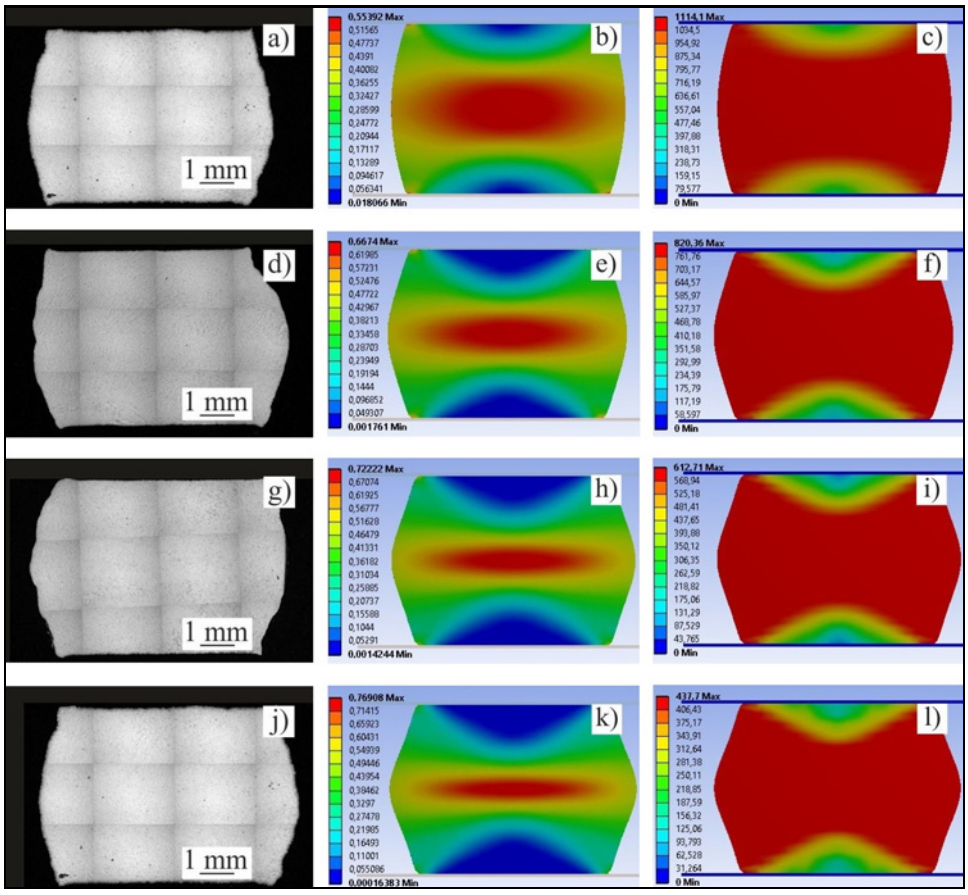

Fig. 11. Longitudinal sections of the barrelled compression specimens and the results of 3D numerical modelling of the barrelled shapes, equivalent plastic strains and stresses at: (a, b, c) 750 °C; (d, e, f) 800 °C; (g, h, i) 850 °C, and (j, k, l) 900 °C.

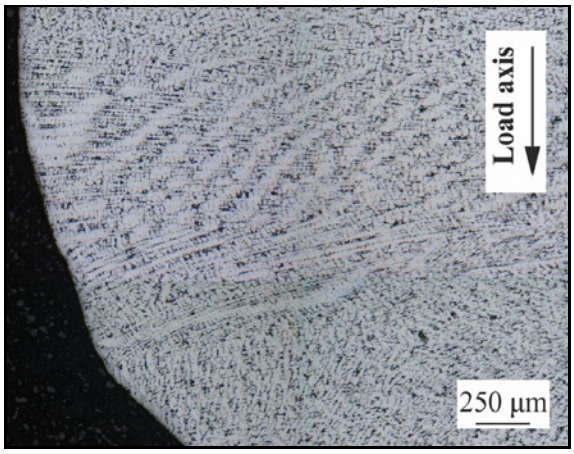

Fig. 12. Formation of protuberances on the surface of the compression specimen tested at 800 °C.

fer from the calculated ones. Figures 11b,e,h,k indicate the inhomogeneous distribution of the local calculated strains. The highest strains are distributed in the central region of the barrelled specimens. The increase of the test temperature leads to a more narrow region of the maximum local strains and a smaller radius of the barrelling. Besides the regions in the vicinity of the contact surfaces, the distribution of the equivalent stresses is relatively homogeneous within the specimens, as shown in Figs. 11c,f,i,l.

3.5. Microstructure after compression

Figure 11 indicates that the contour curves of the barrelled compression specimens are irregular and differ significantly from those calculated by the FEA. The contour curves contain multiple visible protuberances which can be related to the individual columnar grains, as seen in Fig. 12. The straining along the grain boundary between two neighbouring columnar grains lags behind the deformation propagation within the individual grains. The straining behaviour of the grain boundaries indicates their effective strengthening by the intermetallic and ceramic phases (see Figs. 4a,b) which hinder easy boundary sliding. The constrained deformation within the individual grains propagates more easily because the equal straining assuring the integrity of the grain boundary (no grain boundary decohesion or fracture) is not a limiting criterion anymore. The strains within the individual grains are non-uniform and lead to the observed macroscopic protuberances well visible on the surface of the deformed specimens (see Figs. 8 and 11). The strong influence of the anisotropic microstructure on the formation of asymmetric barrelled shapes of the studied CCA is strongly experimentally supported by the barrelling behaviour of the benchmark fine-grained ferritic-pearlitic steel [10, 11] with fcc crystal structure during the compression deformation at 800 °C. The barrelled surface of the benchmark specimen is smooth and the shape is symmetric after the compression test carried out under the identical experimental conditions (specimen size, surface quality, heating conditions, temperature, and strain rate) which have been applied for the compression testing of the CCA specimens at 800 °C, as shown in Figs. 8, 11 and 12.

Figure 13 shows microstructures of the barrelled compression specimens. Numerical simulations in Fig. 11 indicate that the local strain and stress distributions are non-uniform. The lowest local strains and stresses are calculated in the vicinity of the contact surfaces. Figures 13a,d,g,j show that the local stress-strain conditions at the distance of 1 mm from the contact surface have a negligible effect on the secondary phases. On the contrary, local stress-strain conditions in the central region of the specimens lead to the fragmentation of brittle Cr-rich elongated particles (phase 3) and to an intensive plastic deformation of the matrix and other ductile phases designated as 2 and 5 (Table 1), as seen in Figs. 13b,e,h,k. The fragmentation of Cr-rich particles qualitatively corresponds quite well to the numerical calculations of high local stresses and strains. The high local stresses and strains at a distance of 2 mm from the barrelled surface at the position corresponding to d_b lead to the fragmentation of Cr-rich particles only at the test temperatures of 750–850 °C, as seen in Figs. 13c,f,i,l. The number of fragmented particles decrease with increasing test temperature, and no fragmentation is observed at 900 °C. These results indicate that the hot working process can be applied without degradation of brittle reinforcing phases in the studied CCA when an optimal combination of processing parameters is selected.

4. Conclusions

The effect of anisotropic as-cast microstructure on high-temperature compression deformation of multiphase $Co_{24}Cr_{19}Fe_{24}Ni_{19}Al_8(Ti,Si,C)_6$ (at.%) CCA derived from a single phase CoCrFeNi based HEA was studied. The achieved results can be summarised as follows:

1. The microstructure of the as-cast CCA prepared by induction melting and gravity casting consists of columnar and equiaxed grain regions. The primary solidification phase is a solid solution with a cubic crystal structure, and four secondary phases are formed preferentially in the interdendritic region during solidification.

2. The initial multiphase microstructure of the studied compression specimens is highly anisotropic and consists of several columnar grains with [100] crys-

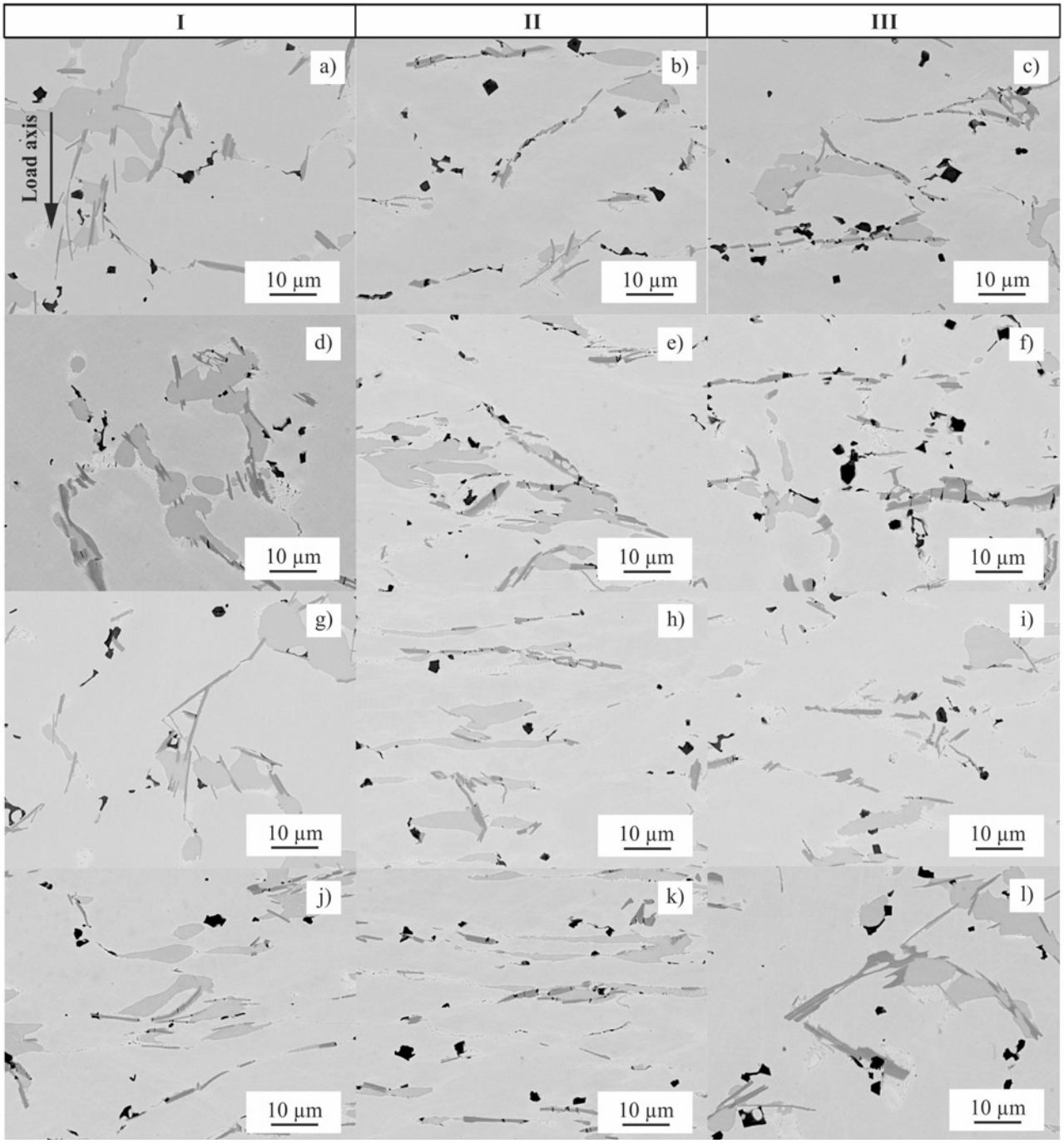

Fig. 13. The microstructure of the specimens after the compression tests at: (a, b, c) 750 °C; (d, e, f) 800 °C; (g, h, i) 850 °C, and (j, k, l) 900 °C. I – 1 mm from the contact surface; II – centre of the specimen; III – position 2 mm from the barrelled surface at the position of d_b. The arrow in Fig. 13a indicates the load axis and is valid for all figures.

tallographic direction parallel or nearly parallel to the load axis.

3. The measured compression deformation curves exhibit work hardening stage which is followed by a steady-state deformation at a constant flow stress. The flow stress depends strongly on the test temperature. The WHR first increases sharply with increasing strain. After achieving a peak value, the WHR decreases and achieves values around zero corresponding to the steady-state deformation.

4. The experimental barrelled shapes differ from the numerically calculated ones. The compression specimens exhibit asymmetric barrelling behaviour. The multiple protuberances on the deformed surfaces result from the anisotropic microstructure of the compression specimens.

5. Local microstructure features such as the fragmentation of brittle phase and plastic deformation of the ductile phases can be qualitatively related to 3D numerical modelling of local strains and stresses within the barrelled specimens.

Acknowledgements

This work was financially supported by the Slovak Grant Agency for Science under the contract VEGA 2/0125/16. The experimental work was carried out thanks to the infrastructure supported by the Research and Development Operational Program funded by the European Regional Development Fund in the frame of the projects: Competence Center for New Materials, Advanced Technologies and Energy (ITMS 26240220073), Center for Applied Research of New Materials and Technology Transfer (ITMS 26240220088), and Center of Applied Research ALLEGRO (ITMS 26220220198).

References

[1] Miracle, D. B., Senkov, O. N.: Acta Mater., *122*, 2017, p. 448. doi:10.1016/j.actamat.2016.08.081
[2] Miracle, D. B.: Mater. Sci. Technol., *31*, 2015, p. 1142. doi:10.1179/1743284714Y.0000000749
[3] Miracle, D. B., Majumdar, B., Wertz, K., Gorsse, S.: Scripta Mater., *127*, 2017, p. 195. doi:10.1016/j.scriptamat.2016.08.001
[4] Gorsse, S., Miracle, D. B., Senkov, O. N.: Acta Mater., *135*, 2017, p. 177. doi:10.1016/j.actamat.2017.06.027
[5] Miracle, D. B., Miller, J. D., Senkov, O. N., Woodward, C., Uchic, M. D., Tiley, J.: Entropy, *16*, 2014, p. 494. doi:10.3390/e16010494
[6] Liu, W. H., Lu, Z. P., He, J. Y., Luan, J. H., Wang, Z. J., Liu, B., Liu, Y., Chen, M. W., Liu, C. T.: Acta Mater., *116*, 2016, p. 332. doi:10.1016/j.actamat.2016.06.063
[7] Fu, Z., Chen, W., Wen, H., Zhang, D., Chen, Z., Zheng, B., Zhou, Y., Lavernia, E. J.: Acta Mater., *107*, 2016, p. 59. doi:10.1016/j.actamat.2016.01.050
[8] Tsai, M.-H., Yeh, J.-W.: Mater. Res. Lett., *2*, 2014, p. 107. doi:10.1080/21663831.2014.912690
[9] He, J. Y., Wang, H., Huang, H. L., Xu, X. D., Chen, M. W., Wu, Y., Liu, X. J., Nieh, T. G., An, K., Lu, Z. P.: Acta Mater., *102*, 2016, p. 187. doi:10.1016/j.actamat.2015.08.076
[10] Štamborská, M., Lapin, J., Bajana, O., Losertová, M.: Kovove Mater., *53*, 2015, p. 399. doi:10.4149/km_2015_6_399
[11] Štamborská, M., Lapin, J., Bajana, O.: Kovove Mater., *54*, 2016, p. 397. doi:10.4149/km_2016_6_397
[12] Štamborská, M., Losertová, M., Konečná, K., Mareš, V., Horsák, L.: Kovove Mater., *53*, 2015, p. 305. doi:10.4149/km_2015_5_305
[13] Wang, X., Li, H., Chandrashekhara, K., Rummel, S. A., Lekakh, S., Van Aken, D. C., O'Malley, R. J.: J. Mater. Process. Tech., *243*, 2017, p. 465. doi:10.1016/j.jmatprotec.2017.01.012
[14] Bennett, C. J., Leen, S. B., Williams, E. J., Shipway, P. H., Hyde, T. H.: Comp. Mater. Sci., *50*, 2010, p. 125. doi:10.1016/j.commatsci.2010.07.016
[15] Wenwen Peng, Weidong Zeng, Qingjiang Wang, Qinyang Zhao, Hanqing Yu: Mater. Sci. Eng. A, *593*, 2014, p. 16. doi:10.1016/j.msea.2013.07.086
[16] Kobayashi, S., Oh, S. I., Altan, T.: Metal Forming and the Finite-Element Method. Oxford, Oxford University Press 1989.
[17] Roebuck, B., Lord, J. D., Brooks, M., Loveday, M. S., Sellars, C. M., Evans, R. W.: Materials High Temp., *23*, 2006, p. 59. doi:10.1179/mht.2006.005
[18] Kúdela Jr., S., Švec, P., Bajana, O., Orovčík, Ľ., Ranachowski, P., Ranachowski, Z.: Kovove Mater., *54*, 2016, p. 483. doi:10.4149/km_2016_6_483
[19] Liu, W. H., Yang, T., Liu, C. T.: Mater. Chem. Phys., 2017. (In press). doi:10.1016/j.matchemphys.2017.07.037
[20] Wagner, A., Shollock, B. A., McLean, M.: Mater. Sci. Eng. A, *374*, 2004, p. 270. doi:10.1016/j.msea.2004.03.017
[21] Lapin, J.: Kovove Mater., *40*, 2002, p. 209.
[22] Lapin, J.: Intermetallics, *5*, 1997, p. 615. doi:10.1016/S0966-9795(97)00035-6
[23] Kurz, W., Fisher, D. J.: Fundamentals of Solidification. 4th Revised Edition. Aedermannsdorf, Trans Tech Publications, Switzerland, 1988.
[24] Wang, F., Ma, D., Bogner, S., Bührig-Polaczek, A.: J. Alloys Compd., *647*, 2015, p. 528. doi:10.1016/j.jallcom.2015.04.237
[25] Zhang, C., Zhang, F., Diao, H., Gao, M. C., Tang, Z., Poplawsky, J. D., Liaw, P. K.: Mater. Des., *109*, 2016, p. 425. doi:10.1016/j.matdes.2016.07.073
[26] Joseph, J., Stanford, N., Hodgson, P., Fabijanic, D. M.: J. Alloys Compd., *726*, 2017, p. 885. doi:10.1016/j.jallcom.2017.08.067
[27] Wang, J., Liu, Y., Liu, B., Wang, Y., Cao, Y., Li, T., Zhou, R.: Mater. Sci. Eng. A, *689*, 2017, p. 233. doi:10.1016/j.msea.2017.02.064
[28] Samal, S., Rahul, M. R., Kottada, R. S., Phanikumar, G.: Mater. Sci. Eng. A., *664*, 2016, p. 227. doi:10.1016/j.msea.2016.04.006
[29] Ebrahimi, R., Najafizadeh, A.: J. Mater. Process. Technol., *152*, 2004, p. 136. doi:10.1016/j.jmatprotec.2004.03.029
[30] Wu, Z., Troparevsky, M. C., Gao, Y. F., Morris, J. R., Stocks, G. M., Bei, H.: Curr. Opin. Solid State Mater. Sci., 2017. (In press). doi:10.1016/j.cossms.2017.07.001
[31] Diao, H. Y., Feng, R., Dahmen, K. A., Liaw, P. K.: Curr. Opin. Solid State Mater. Sci. (2017). (In press). doi:10.1016/j.cossms.2017.08.003
[32] Seok, K., Kang, J., Ram, K., Sang, Y.: Mater. Charact., *132*, 2017, p. 162. doi:10.1016/j.matchar.2017.08.010